

Spherical indentation response of metallic glasses

M.N.M. Patnaik^a, R. Narasimhan^{b,*}, U. Ramamurty^c

^a ISRO Satellite Centre, Bangalore 560017, India

^b Department of Mechanical Engineering, Indian Institute of Science, Bangalore 560012, India

^c Department of Metallurgy, Indian Institute of Science, Bangalore 560012, India

Received 24 December 2003; received in revised form 15 March 2004; accepted 21 March 2004

Available online 20 April 2004

Abstract

Metallic glasses exhibit high hardness values, typified by a plastic constraint factor (the ratio of hardness to compressive yield strength) that is considerably larger than that seen in ductile crystalline metals. The reason for this behaviour is investigated in this paper, by conducting a combined experimental and numerical study on the spherical indentation response of a Zr-based bulk metallic glass (Vitreyloy-1). An extended Drucker–Prager constitutive theory with different levels of pressure sensitivity is employed in the numerical simulations. In addition, a modified version of the expanding cavity model, which incorporates pressure sensitivity of yielding, is used to interpret the trends exhibited by the experimental and computational results. Attention is focused on the development of plastic flow beneath the indenter as well as the variation of hardness with indentation strain. It is shown that the high plastic constraint factor exhibited by metallic glasses at large indentation strains is an outcome of their pressure sensitive plastic deformation. These observations are discussed in the context of an appropriate constitutive model for yielding of metallic glasses. © 2004 Acta Materialia Inc. Published by Elsevier Ltd. All rights reserved.

Keywords: Metallic glasses; Indentation; Hardness; Plastic deformation; Finite element analysis

1. Introduction

Metallic glasses exhibit a unique combination of mechanical properties. At low temperatures (less than about half the glass transition temperature), after a relatively large elastic deformation (of about 2%), plasticity ensues with strain localization into narrow bands resulting in inhomogeneous deformation [1]. In uniaxial tension, catastrophic fracture occurs immediately after yielding, due to the absence of barriers (such as grain boundaries) for shear band propagation. On the other hand, under uniaxial compression, significant plastic deformation is observed with little strain hardening (i.e., an almost elastic-perfectly plastic response) [1].

At the macroscopic level, the constitutive law that best describes yielding in metallic glasses, has been a subject of considerable research [2–11]. A consensus is emerging that the von Mises yield criterion, which is

useful in describing the plastic behavior of ductile metals accurately, is inadequate in capturing the yield behavior of the metallic glasses. Instead, it has been suggested that a Mohr–Coulomb type yield criterion, which takes the normal stress across the slip plane in addition to the local shear stress into account, is better suited [6,7].

Indentation tests can provide insights into the multi-axial deformation characteristics of materials that are being tested. Consequently, the hardness and indentation response of a number of metallic glasses (both the rapidly-quenched and bulk metallic glasses) has been studied and reported in literature. An interesting observation that can be made from these studies is that the hardness of a variety of metallic glasses is between 3 and 4.5 times the compressive yield strength σ_0^c [12–15]. This is much higher than that for crystalline metals which is utmost $3\sigma_0^c$ [16]. A possible factor contributing to this discrepancy is the pressure sensitivity of yielding. Narasimhan [17] has recently modified the expanding cavity model of Johnson [18] to study the conical and spherical indentation response of pressure sensitive plastic solids and predicted that the hardness increases

* Corresponding author. Tel.: +91-80-22932959; fax: +91-80-23600648.

E-mail address: narasi@mecheng.iisc.ernet.in (R. Narasimhan).

strongly with the pressure sensitivity index of the material.

The aim of the present work is to critically examine the reason for the relatively high constraint factor observed in metallic glasses. In particular, the effect of the constitutive behaviour on the indentation response of metallic glasses is studied. Attention is focussed on spherical indentation for the following reasons. First, instrumented spherical indentation allows for monitoring the hardness as a function of the indentation strain which is given by the ratio of contact radius a to indenter radius R [16,18]. This facilitates for the examination of the indented material's response in the elastic, elastic–plastic and fully plastic regimes. Second, because of the axisymmetry, the results can be interpreted using simple analytical models such as the expanding cavity model [17,18]. Further, axisymmetric finite element simulations can be performed to analyse the experiments instead of expensive 3D computations as in the case of Vickers or Berkovich indentation [7,19].

In this paper, finite element simulations of spherical indentation of a metallic glass that obeys the extended Drucker–Prager (EDP) yield criterion [20] are conducted and the results are compared with experimental measurements as well as with predictions based on the modified expanding cavity model [17]. The extended Drucker–Prager constitutive equations can be reduced to either the von Mises or the original Drucker–Prager model by appropriate choice of material parameters [20]. Further, it can be made to closely approximate the Mohr–Coulomb yield function with proper selection of these parameters. In this connection, it must be mentioned that Vaidyanathan et al. [7] and Giannakopoulos and Larsson [19] analyzed the mechanics of Berkovich and Vickers indentation of elastic–plastic specimens which obey the Mohr–Coulomb and the original Drucker–Prager constitutive models, respectively. While the former work is aimed at identifying the constitutive response of bulk metallic glasses, the latter examines the Vickers indentation behaviour of elastic–plastic solids. By contrast, attention is focussed in the present study on the effect of the yield response on the variation of indentation load with depth, development of plastic flow and stress distribution in a metallic glass specimen during spherical indentation. Further, the variation of hardness with indentation strain is investigated.

2. Material and experiments

Instrumented indentation experiments on a Zr-based bulk metallic glass with a composition of $Zr_{41}Ti_{14}Ni_{10}Cu_{12.5}Be_{22.5}$ (Vitreloy-1) were performed. The processing and property details of this material can be found in [11]. A plate specimen with a thickness of 3 mm and a width of 4 mm was utilized for the indentation experi-

ments. Prior to indentation, the sides of the specimens that are to be indented were polished by successive polishing steps to a 1 μm finish using diamond paste. Indentation experiments were conducted using an instrumented microindenter (Micro Hardness Tester, CSM Instruments, Switzerland) that utilizes a feedback control force actuator to ensure rigid displacement control during loading and a differential capacitive technique for precise measurement of indentation depth. The displacement measured is that between the indenter tip and a reference plate placed close (within 0.5 mm) to the specimen, so that the influence of the machine compliance on the load versus depth curve gets nullified. The indenter is capable of 200 μm maximum displacement with a resolution of 0.3 nm and a maximum load of 30 N with a load resolution of 0.3 mN.

The load versus depth data are continuously acquired with an attached computer and the built-in software facilitates obtaining different parameters like stiffness of the unloading curve, contact depth, etc. Additionally, the software analyzes the data with the methodology developed by Oliver and Pharr [21] and estimates the mechanical properties like hardness and elastic modulus. Using a spherical diamond indenter of radius $R = 50 \mu\text{m}$, indentations were made with maximum loads of 1, 5, 10 and 20 N. At each load, the loading and unloading rates were maintained at 2 N/min and a 15 s

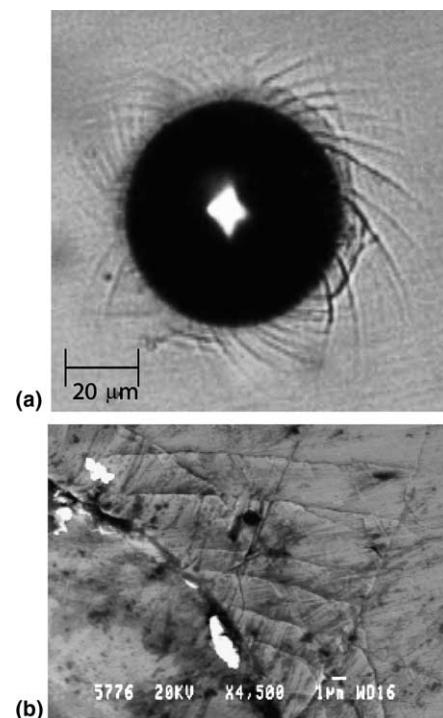


Fig. 1. (a) Optical micrograph of the spherical indentation impression made with a maximum indentation load of 20 N, showing shear bands emanating from the edge of the impression. (b) High magnification scanning electron micrograph of a region at the edge of an indent showing two intersecting families of slip lines.

hold time was allowed at the maximum load to minimize any inertial effects of the machine. No creep was observed during the hold period. At least five experiments were conducted for each case and the results were found to be highly reproducible.

The impressions were imaged subsequent to the indentation experiments using optical as well as scanning electron microscopes. Fig. 1(a) shows an optical micrograph of the spherical indent made with a maximum load of 20 N. The diameter of the residual impression is around 64 μm . Flow lines, emanating from the edge of the indentation impression, are seen. Interestingly, these appear to resemble the slip lines around a pressurised circular hole in a perfectly plastic solid under plane strain which are logarithmic spirals [22]. Atomic force microscopy (AFM) was utilized to ascertain that these flow lines are shear bands and not cracks. Fig. 1(b) is a scanning electron micrograph showing a higher magnification view of a region adjacent to the edge of contact. A network of two families of slip lines can be seen. The included angle between these two families of slip lines is found to be on the average around 79°.

Fig. 2(a) shows an AFM image of the shear banded region at the edge of the indent. In Fig. 2(b), a line scan across several shear bands (dotted arrow in Fig. 2(a)) is presented displaying the topology of the surface. From this figure, it is seen that the discrete displacement jump at the surface associated with the shear bands varies between 30 and 100 nm. This observation is consistent with the discrete displacement jumps observed during low velocity nanoindentation as well as macroindentation experiments on a variety of metallic glasses [13,15].

3. Numerical analysis

3.1. Constitutive equations

As mentioned in the introduction, the EDP yield criterion is employed in the computations carried out in this work. From the standpoint of a numerical formulation, it is easier to implement this yield function (as compared to the Mohr–Coulomb criterion) because it has a continuously varying normal.

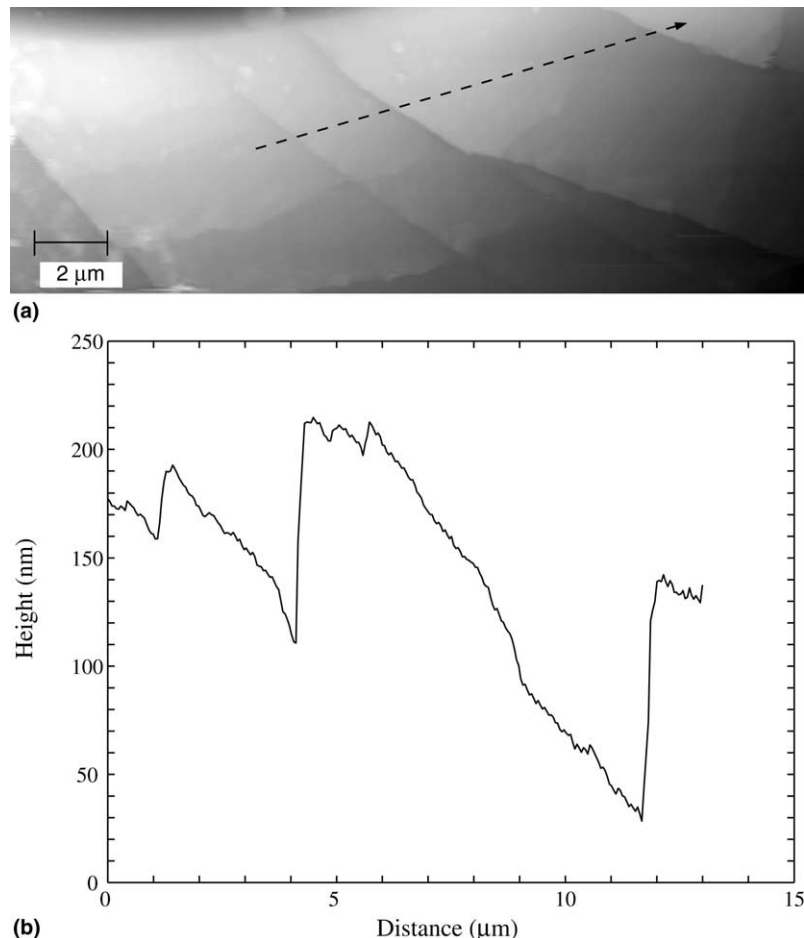


Fig. 2. (a) An AFM image of the shear-banded region around the edge of an indent. The arrow indicates the line scan, topology of which is shown in (b).

The EDP yield function is given as (see [20])

$$\Phi(\sigma_{ij}, \sigma^c) = \frac{q}{2} \left[1 + \frac{1}{\mathcal{C}} - \left(1 - \frac{1}{\mathcal{C}} \right) \left(\frac{r}{q} \right)^3 \right] + \sigma_m \tan \alpha - \left(1 - \frac{1}{3} \tan \alpha \right) \sigma^c = 0, \quad (1)$$

where

$$\sigma_m = \frac{1}{3}(\sigma_1 + \sigma_2 + \sigma_3), \quad (2)$$

$$q = \sqrt{(3J_2)}, \quad (3)$$

and

$$r^3 = \frac{27}{2} J_3. \quad (4)$$

Here, $(\sigma_1, \sigma_2, \sigma_3)$ are the principal values of the Cauchy stress tensor σ_{ij} , J_2 and J_3 are the second and third invariants of the deviatoric part of the Cauchy stress, and σ_m is the hydrostatic stress. Further, σ^c is the true yield stress in a uniaxial compression test and α (which is referred to as the pressure sensitivity index) and \mathcal{C} are material parameters. The yield function described by Eq. (1) represents a conical surface in principal stress space with the vertex on the hydrostatic tension axis. The trace of the yield surface on the deviatoric plane is non-circular and its shape is determined by the parameter \mathcal{C} . A circular trace is obtained for the special case of $\mathcal{C} = 1$ which corresponds to the original Drucker–Prager model. To ensure convexity of the yield surface, \mathcal{C} must be greater than 0.778 [20]. It must be noted that for the special case of $\mathcal{C} = 1$ and $\alpha = 0^\circ$, Φ in Eq. (1) reduces to the von Mises yield function.

The total deformation rate D_{ij} (symmetric part of the spatial gradient of velocity) is taken to be the sum of an elastic and a plastic part, so that

$$D_{ij} = D_{ij}^e + D_{ij}^p. \quad (5)$$

The Jaumann rate of Cauchy stress σ_{ij}^* is related to D_{ij}^e by a constant, positive definite, isotropic elasticity tensor C_{ijkl} as

$$\sigma_{ij}^* = C_{ijkl} D_{kl}^e. \quad (6)$$

In this work, an associated flow rule is employed so that the plastic part of the deformation rate D_{ij}^p is taken to be directed along the normal to the yield surface. In order to describe the strain hardening behavior for multiaxial loading, an effective plastic strain increment is defined as

$$d\bar{\epsilon}^p = \frac{(1 - \frac{1}{3} \tan \alpha)}{\sqrt{\frac{3}{2} + \frac{1}{3} \tan^2 \alpha}} \sqrt{D_{ij}^p D_{ij}^p} \quad (7)$$

so that it reduces to the axial plastic strain increment under uniaxial compression. On employing Eq. (6) along with the flow rule and the plastic consistency condition, the rate constitutive equation can be derived as

$$\sigma_{ij}^* = L_{ijkl} D_{kl}, \quad (8)$$

where L_{ijkl} is the elastic–plastic constitutive tensor.

The response of the material in uniaxial compression is idealized by a piecewise power hardening law of the form:

$$\frac{\epsilon^c}{\epsilon_0^c} = \begin{cases} \sigma^c / \sigma_0^c, & \sigma^c \leq \sigma_0^c, \\ (\sigma^c / \sigma_0^c)^n, & \sigma^c > \sigma_0^c. \end{cases} \quad (9)$$

Here, σ_0^c is the initial yield stress and $\epsilon_0^c = \sigma_0^c / E$ is the initial yield strain under uniaxial compression and n is the strain hardening exponent of the material. In the present computations, n is assumed as 20 to represent the almost perfectly plastic behaviour of metallic glasses. Further, the initial compressive yield strain σ_0^c / E and Poisson's ratio ν are chosen as 0.02 and 0.36, respectively, which correspond to the properties reported in [7] for Vitreloy-1. Three values of $\alpha = 0^\circ, 10^\circ$ and 20° are considered. These are realistic since previous investigations [6,7] suggest values for the Mohr–Coulomb friction parameter corresponding to Pd- and Zr-based metallic glasses in the range from 0.08 to 0.14 which are approximately equivalent to $\alpha = 9\text{--}17^\circ$ for the EDP model. Most of the computations are carried out for the case of $\mathcal{C} = 1$. However, for $\alpha = 10^\circ$, results are also reported for $\mathcal{C} = 0.8$ in order to assess the effect of shape of the yield locus on the indentation response.

3.2. Computational aspects

In this work, axisymmetric finite element analyses of spherical indentation of a cylindrical specimen are conducted. An updated Lagrangian finite element formulation [23] is employed. The contact between the rigid indenter and the specimen is assumed as frictionless and is modelled using the slideline approach along with a penalty formulation [24]. The finite element mesh used in the computations is shown in the r – z plane along with the applied boundary conditions and the rigid indenter at incipient contact in Fig. 3. It is comprised of 1488 four-noded isoparametric quadrilateral elements and is well refined near the zone of indentation. It was chosen on the basis of a mesh convergence study in order to ensure that the results reported below are only marginally affected by further refinement of the mesh. The ratio of the specimen radius to indenter radius L_s/R and specimen depth to indenter radius d_s/R are taken as 6 and 5, respectively. The simulations are carried out under displacement controlled conditions till a maximum indentation depth of $0.2R$ is attained. At this stage, the maximum plastic zone extent in the specimen is confined to within $2R$, so that there is no interaction with the specimen boundaries.

It must be noted that since a continuum analysis with homogeneous material properties is performed here, the results would depend only on the ratios of different

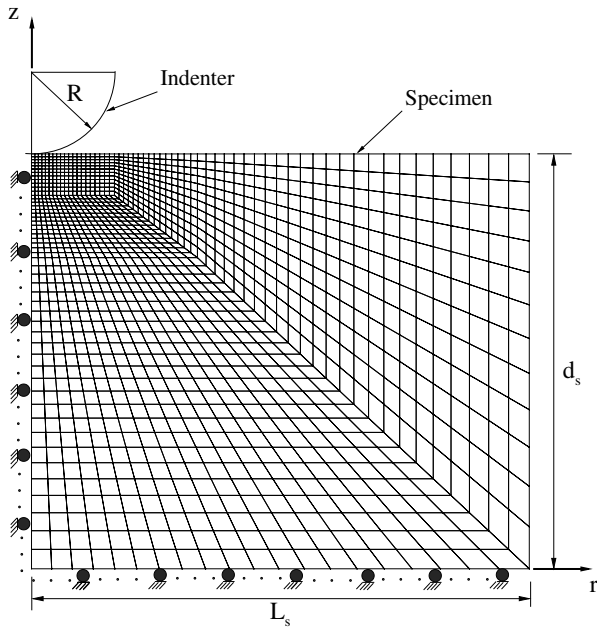


Fig. 3. Finite element mesh of the specimen in the r - z plane along with boundary conditions and the rigid indenter.

length dimensions and not on their absolute values. Thus, for example, from analytical solutions for contact between a sphere and an elastic or elastic-plastic half-space [25,26], as well as from dimensional requirements, it may be expected that the indentation load P would have the following functional form:

$$P = ER^2 f(h/R, \sigma_0^c/E, n, \alpha, C, \nu). \quad (10)$$

In the above equation, h/R is the ratio of the indentation depth to indenter radius. Here, it is assumed that the plastic zone is small enough and does not interact with the specimen boundaries. In view of above considerations, all results are presented below in an appropriately normalized form.

4. Results

4.1. Variation of load with indentation depth

The variations of normalized load $P/(ER^2)$ with indentation depth h/R corresponding to different values of material parameters C and α are presented in Fig. 4. Also shown are the unloading curves corresponding to two stages of indentation ($h/R = 0.1$ and 0.2). The P - h curve predicted by the elastic Hertz solution, which is given by $P/(ER^2) = 4/(3(1 - \nu^2))(h/R)^{3/2}$ [26], and the experimental data pertaining to Vitreloy-1 are included in Fig. 4 for comparison. At small loads, the numerically obtained P - h curves merge with the elastic Hertz solution. The elastic modulus of about 95 GPa, estimated from the unloading slopes of the experimental as well as

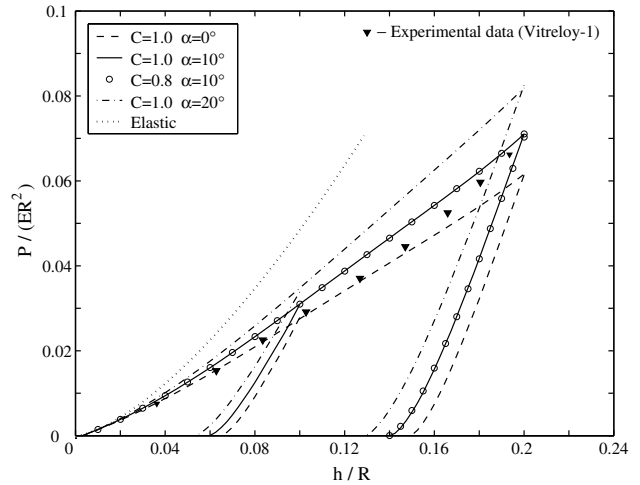


Fig. 4. Normalized load versus indentation depth curves corresponding to different values of material parameters obtained from numerical simulations along with experimental data for Vitreloy-1.

computed P - h curves, is consistent with the value reported in literature for Vitreloy-1.

The P - h curves computed from the elastic-plastic analyses become almost linear at large h/R . In order to confirm this observation, variations of the type $P/(ER^2) = A(h/R)^s$, where A is a constant, were fitted to the loading curves corresponding to different ranges of indentation depth. It was found that the index s decreases from around 1.5 at small h/R to a value of about 1.1 at $h/R = 0.2$. In this connection, it must be noted that the expanding cavity model [25] for indentation of an elastic-perfectly plastic solid assumes a linear variation of load with indentation depth under fully plastic conditions.

On examining the different loading curves shown in Fig. 4, it can be noted that the load at a given h/R increases with α . Thus, the von Mises model ($\alpha = 0$) predicts the lowest load versus indentation depth response. The reason for the above behaviour is the higher compressive axial stress experienced by the material underneath the indenter when α increases as will be discussed later. The experimental P - h data for Vitreloy-1 lies between the curves pertaining to $\alpha = 0^\circ$ and 10° . On following the unloading curves, it can be seen that the ratio of residual depth at complete unloading to the value at the beginning of unloading, h_r/h_{max} , decreases with increase in α . In order to clearly illustrate this trend, the above ratio is plotted against the indentation strain normalized by the compressive yield strain, $Ea/(\sigma_0^c R)$, in Fig. 5 corresponding to different combinations of material parameters. The experimental data for h_r/h_{max} corresponding to Vitreloy-1, which is included in this figure, is lower than that predicted by the von Mises model.

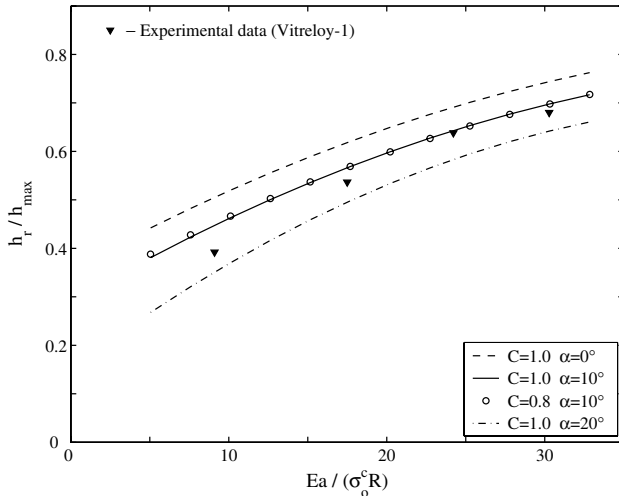


Fig. 5. Ratio of residual depth at complete unloading to the value at the beginning of unloading, h_r/h_{\max} , versus normalized indentation strain, $Ea/(\sigma_0^c R)$ corresponding to different values of material parameters obtained from numerical simulations along with experimental data for Vitreloy-1.

The above observations pertaining to the influence of α on the P - h response are qualitatively similar to the results of Vaidyanathan et al. [7] and Giannakopoulos and Larsson [19] for Berkovich and Vickers indentation.

By contrast, it is interesting to note from Figs. 4 and 5 that the shape parameter \mathcal{C} of the yield locus has little influence on the P - h curve as well as on the variation of h_r/h_{\max} with indentation strain.

4.2. Development of plastic flow

The plastic zone development in the specimen at different stages of indentation, as characterized by the levels of indentation strain a/R , for the material with $\mathcal{C} = 1$ and $\alpha = 10^\circ$ is depicted in normalized coordinates in Fig. 6. It can be seen from this figure that the plastic zone at initial stages of indentation is elongated in the axial direction, whereas it becomes more rounded (i.e., hemispherical) at large indentation strain (as fully plastic conditions are approached). Thus, in Fig. 6, the ratio of the plastic zone extent in the axial direction to that in the radial direction, r_{pz}/r_{pr} , is around 1.9 at $a/R = 0.26$, whereas it reduces to 1.2 at $a/R = 0.58$. In this context, it must be noted that the expanding cavity model [17,18] assumes a hemispherical plastic zone surrounding the center of contact at the specimen surface.

The variations of normalized plastic zone size in the axial direction, r_{pz}/R , with normalized indentation strain, $Ea/(\sigma_0^c R)$, are shown in Fig. 7(a) corresponding to different material parameters. It is important to note that the plastic zone size at a given indentation strain increases strongly with α . This correlates with the larger indentation load experienced by a material with higher α

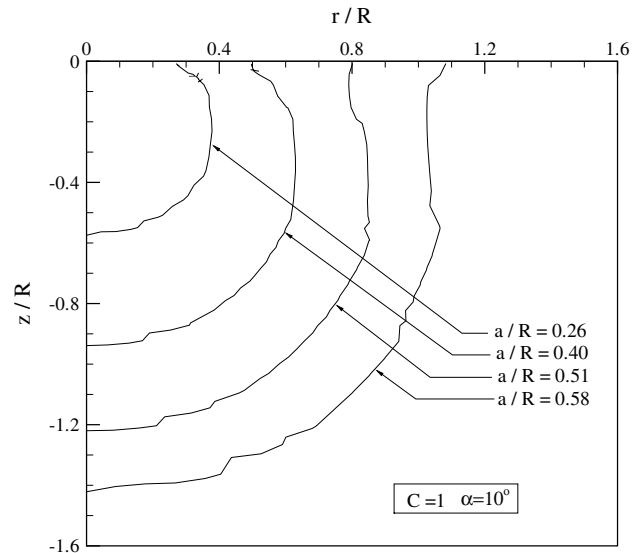


Fig. 6. Development of plastic zone in the specimen with indentation for the material with $\alpha = 10^\circ$.

as mentioned earlier. A similar observation based on the expanding cavity model was made by Narasimhan [17]. Indeed, the elastic-plastic solution for an internally pressurised spherical cavity obtained by Narasimhan [17] shows that the plastic zone surrounding the cavity grows by a larger amount for a given increment in radial displacement of the cavity boundary when α is higher. Also, as in the case of the P - h curves, it can be noticed from Fig. 7(a) that the yield locus shape parameter \mathcal{C} has little influence on the growth of the plastic zone size in the specimen.

In Fig. 7(b), the evolution of the normalized plastic zone extents in the axial and radial directions, r_{pz}/R and r_{pr}/R with normalized indentation strain obtained from the finite element analyses (FEA) are shown for the case of $\alpha = 10^\circ$. Also displayed is the corresponding variation based on the expanding cavity model (ECM) derived by Narasimhan [17] (see also Appendix A). Fig. 7(b) shows that the plastic zone radius predicted by the cavity model lies in between the axial and the radial plastic zone extents computed from FEA. Further, it can be seen that r_{pr} approaches r_{pz} at large indentation strain as noted from Fig. 6.

4.3. Contact stress distribution

The distribution of normalized axial stress σ_{zz}/σ_0^c along the contact zone (i.e., just beneath the indenter) is shown in Fig. 8 corresponding to various material properties at a normalized indentation strain, $Ea/(\sigma_0^c R) = 30$. It can be seen from this figure that the axial stress distribution on the contact zone, obtained from the elastic-plastic analyses, is quite uniform and drops sharply in magnitude at the edge of contact which is different from the elastic

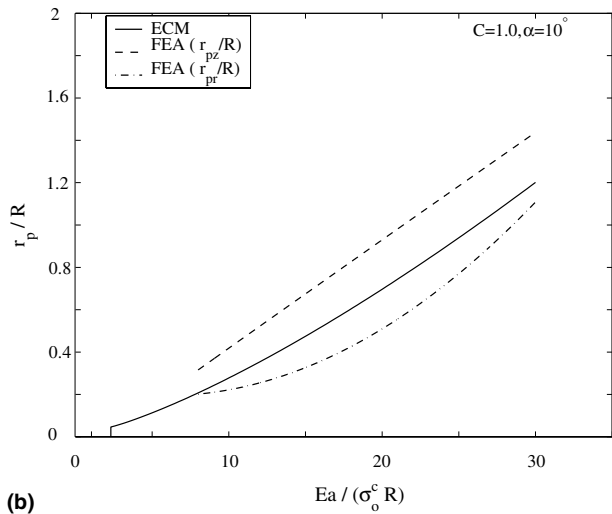
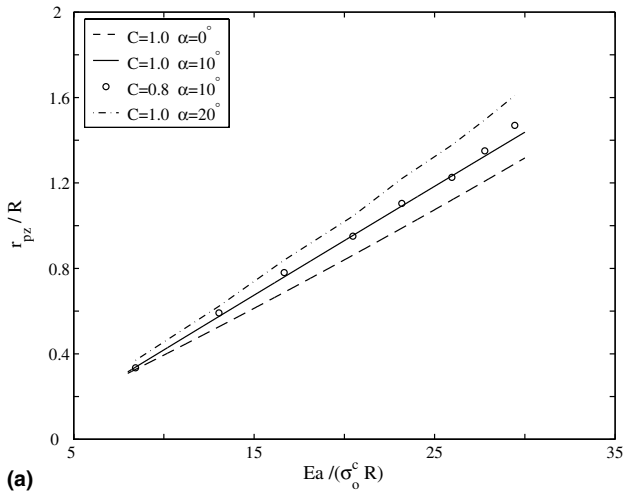


Fig. 7. (a) Variation of normalized plastic zone extent in axial direction with normalized indentation strain. (b) Variation of normalized plastic zone extents in axial and radial directions with normalized indentation strain obtained from finite element analysis (FEA) along with prediction by the expanding cavity model (ECM) for the material with $\alpha = 10^\circ$.

Hertz solution [25]. Similar stress variations have been obtained from FEA by other investigators for materials obeying the von Mises model (see, for example, [27]). Further, it is found from the present computational results that σ_{rr} and $\sigma_{\theta\theta}$ are also compressive and display a uniform variation over a predominant portion of the contact zone.

The average values of all stress components over the contact area at $Ea/(\sigma_0^c R) = 30$ are summarized in Table 1 along with the predictions based on the cavity model. This model assumes that the stress state along the contact zone is given by $\sigma_{zz} = -(p + \hat{\sigma})$ and $\sigma_{rr} = \sigma_{\theta\theta} = -(p - \hat{\sigma}/2)$, where p is the hydrostatic pressure (see Appendix A). The above contention is supported by the computational results which show that the values of σ_{rr} and $\sigma_{\theta\theta}$ on the contact zone are close to each other

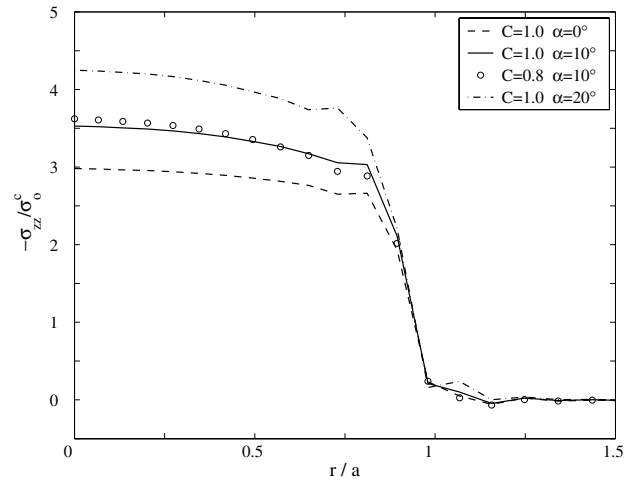


Fig. 8. Axial stress distributions along the contact zone at a normalized indentation strain, $Ea/(\sigma_0^c R) = 30$.

(within 5%, see Table 1). Further, while the average values of σ_{zz} on the contact zone match closely with the results of the cavity model, the latter predicts somewhat lower magnitudes for the radial and circumferential stress components. Notwithstanding this discrepancy, it is important to note from Table 1 and Fig. 8 that both the cavity model and FEA show that the magnitude of all stress components on the contact zone enhance with α . This trend is particularly pronounced for σ_{zz} which increases in magnitude by about 35% as α changes from 0° to 20° . It is attributed to the enhancement in magnitude of both the hydrostatic (or core) pressure p and the superposed compressive axial stress $\hat{\sigma}$ with α (see [17] as well as Eq. (A.11)). The former can be traced to the higher internal pressure which is required to expand a spherical cavity when α is larger [17].

4.4. Variation of hardness with indentation strain

The variation of the normalized hardness H/σ_0^c , also referred to as the constraint factor [26], with normalized indentation strain $Ea/(\sigma_0^c R)$ is shown in Fig. 9 corresponding to different α (with $\mathcal{C} = 1$). The results deduced from FEA are compared with the predictions based on the expanding cavity model [17]. Also included in the figure are the hardness data corresponding to Vitreloy-1 obtained from the spherical indentation experiments conducted in this work as well as the Berkovich hardness value reported in [29]. The equivalent indentation strain corresponding to the latter is taken as $\tan(19.7^\circ)$ [18]. It must first be noted that the hardness predicted by the expanding cavity model and FEA agree well with each other for all values of α and over a wide range of indentation strains. The constraint factor increases strongly with α , particularly at large indentation strain. As explained in Section 4.3, this is primarily

Table 1

Average values of stresses in the contact zone at $Ea/(\sigma_0^c R) = 30$ obtained from finite element analysis (FEA) and the expanding cavity model (ECM) corresponding to different material parameters

ζ	α (°)	FEA			ECM	
		σ_{rr}/σ_0^c	$\sigma_{\theta\theta}/\sigma_0^c$	σ_{zz}/σ_0^c	σ_{rr}/σ_0^c	σ_{zz}/σ_0^c
1.0	0	-1.69	-1.69	-2.56	-1.55	-2.55
0.8	10	-1.84	-1.76	-2.92	-1.65	-2.96
1.0	10	-1.86	-1.83	-2.95	-1.65	-2.96
1.0	20	-2.01	-1.93	-3.45	-1.75	-3.47

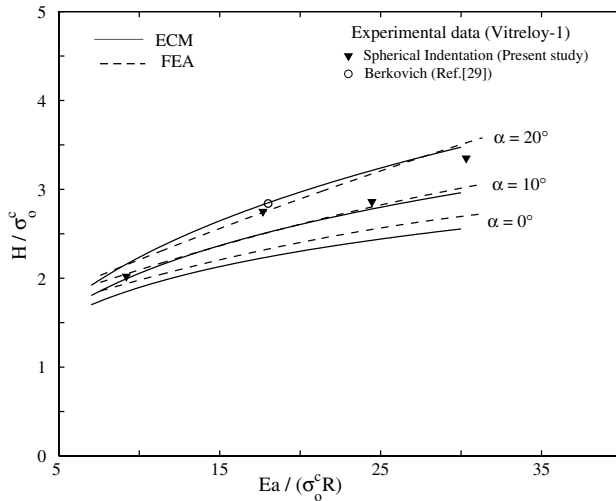


Fig. 9. Variation of normalized hardness with indentation strain predicted by finite element analysis (FEA) and expanding cavity model (ECM) corresponding to different α along with experimental data for Vitreloy-1.

caused by the higher hydrostatic pressure prevailing underneath the indenter when α is larger. The hardness data for Vitreloy-1 (both from the present experiments as well as the Berkovich test reported in [29]) is higher than that predicted by the von Mises model. Further experimental support for this conclusion is provided by the microindentation test results on various Zr- and Pd-based bulk metallic glasses reported in [12,14,15] which show values of hardness exceeding three times the yield strength.

5. Discussion

The elastic–plastic constitutive response of metallic glasses has been investigated in several studies, but is still not fully understood. However, it is now widely recognized that the von Mises yield criterion is inappropriate for metallic glasses even though some experimental evidence in support of this model has been provided by Kimura and Masumoto [8] and Bruck et al. [2]. There are several reasons for this contention. First, the measured values of tensile yield strength for metallic

glasses are found to be lower than the compressive yield strength [6]. Atomistic simulations incorporating shear transformation zones, which are the fundamental units of plasticity in metallic glasses, have also demonstrated this tension–compression asymmetry [10]. Secondly, recent experiments conducted by Lu and Ravichandran [11] show that the yield strength of Vitreloy-1 is strongly influenced by hydrostatic pressure. They employed a confining ring method and were able to subject cylindrical specimens to high hydrostatic pressure (of the order of 2.8 GPa) in addition to axial compression. In this context, it must be noted from the present study that the hydrostatic pressure underneath the indenter is of the order of $2.3\sigma_0^c$ (see Table 1), which is around 4.4 GPa for Vitreloy-1.

Further, it has been reported that the orientation of slip bands under uniaxial compression in some metallic glasses deviates from the plane of maximum resolved shear stress (see, for example [6]). This behaviour is similar to that observed for polymers [30] and implies that both the normal stress as well as the shear stress on the slip plane should influence yielding in metallic glasses. In this connection, as noted in Section 2, the included angle between the two families of slip lines seen around the edge of contact in Fig. 1(b) is 79° . If the material obeys the Tresca or von Mises yield criterion, the slip lines would be the maximum shear directions with an included angle of 90° .

In order to incorporate the above noted observations within the framework of continuum plasticity, the Mohr–Coulomb, modified Tresca and Drucker–Prager yield criteria have been suggested for metallic glasses [6]. The Mohr–Coulomb yield function is given by

$$|\tau| = \tau_0 - \mu\sigma_n, \quad (11)$$

where τ and σ_n are the shear and normal stresses on the slip plane, and τ_0 and μ are the yield stress in pure shear and friction parameter, respectively. The modified Tresca yield function, advocated by Lu and Ravichandran [11], is given by

$$|\tau| = \tau_0 - \beta\sigma_m, \quad (12)$$

where β is a pressure sensitivity index. It is important to recognize that while only the Mohr–Coulomb model can explain the deviation of the slip bands from the maxi-

imum shear stress direction, all the above yield criteria display tension–compression asymmetry [6] as well as hydrostatic stress dependence. Thus, in principal stress space, the Mohr–Coulomb and modified Tresca yield surfaces are (irregular and regular) hexagonal pyramids with vertex on the hydrostatic tension axis [31]. Further, these yield functions are dependent on both J_2 and J_3 , whereas the original Drucker–Prager model does not involve J_3 (and, hence, has a circular trace on the deviatoric plane [31]). The EDP yield function employed in this work incorporates J_3 dependence as well (see Eq. (1)), has a smoothly varying normal, and can be made to closely approximate the Mohr–Coulomb yield function with proper choice of \mathcal{C} and α [20]. It should be noted that an included angle of 79° between the slip lines, as observed in the present experimental study, is representative of a Mohr–Coulomb material with friction parameter of 0.19 [32]. This corresponds to $\alpha \approx 20^\circ$ in the extended Drucker–Prager constitutive model used in this work and is consistent with the hardness measurements as well.

It is important to note that the present simulations have demonstrated that the shape parameter \mathcal{C} of the yield locus has little influence on the spherical indentation response. Indeed, for a spherically symmetric stress field, all the yield criteria mentioned above will coincide, and hence, from the expanding cavity model [17], it follows that they will predict similar indentation behaviour. Thus, in general, it would be difficult to discern from indentation studies, which of the above yield criteria is most suitable for metallic glasses. However, the present work clearly shows that both the hardness and plastic zone size associated with spherical indentation of metallic glasses depend on the yield strength as well as the pressure sensitivity index α of the material. This suggests that results such as those depicted in Figs. 7(a) and 9 can be employed in conjunction with corresponding experimental data for metallic glasses to deduce the values of σ_0^c and α . In this connection, it must be pointed out that in recent studies, plastic zone measurements around nanocontacts have been combined with cavity model predictions to provide reliable estimates of the yield strength for various alloys (see, for example [33]). The present work suggests that such an approach can yield valuable information about the mechanical properties of metallic glasses as well.

6. Summary and conclusions

The main conclusions of this work are summarized below.

1. The load at a given indentation depth increases with the pressure sensitivity index α of the material, whereas the ratio of residual depth at complete unloading to the maximum indentation depth, h_r/h_{\max} ,

decreases. The experimental P – h data for Vitreloy-1 is higher than that predicted by the von Mises model ($\alpha = 0^\circ$). Also, the data for h_r/h_{\max} is lower than that given by this model.

2. The plastic zone surrounding the indented region is initially elongated in the axial direction but becomes more rounded at later stages of indentation. The plastic zone size enhances with α at a given indentation strain which is consistent with the predictions of the expanding cavity model.
3. All stress components underneath the indenter are compressive and display a uniform variation over a predominant portion of the contact zone. The finite element results corroborate the assumptions made in the cavity model about the contact stress distribution (such as $\sigma_{rr} \approx \sigma_{\theta\theta}$). In fact, the average values of the stresses in the contact zone computed from FEA agree well with those predicted by the cavity model. It is important to note that all stress components in the contact zone increase in magnitude with α .
4. The constraint factor H/σ_0^c obtained from the finite element solution is close to that given by the cavity model for a wide range of indentation strain, irrespective of α . It enhances strongly with α particularly at large indentation strain. This is attributed to the higher core pressure required to expand a spherical cavity when α is larger. The experimental constraint factor data for Vitreloy-1 is higher than that predicted by the von Mises model and appears to fall between the values computed for $\alpha = 10^\circ$ and 20° , which is consistent with the included angle measured between the slip lines around the indents.

Acknowledgements

U.R. acknowledges the financial support from DRDO, India. The authors are grateful to Dr. Nicholas Randall and Dr. Richard Soden of CSM Instruments, Switzerland for conducting the instrumented indentation experiments and imaging reported in this paper.

Appendix A. Expanding cavity model for indentation analysis of pressure sensitive plastic solids

In this appendix, an approximate analysis of spherical indentation of pressure sensitive plastic solids by the expanding cavity model is briefly described. The material is assumed to obey the Drucker–Prager yield criterion (Eq. (1) with $\mathcal{C} = 1$) and the associated flow rule. A more detailed description of the cavity model has been presented recently by Narasimhan [17].

The expanding cavity model developed by Marsh [34] and Johnson [18] assumes that the subsurface displacements produced by any blunt indenter are

approximately radial from the point of first contact and the plastic strain contours are hemispherical in shape. The contact surface is taken to be encapsulated in a hemispherical core of radius a (see Fig. 10). It is further assumed that a hydrostatic compressive stress of magnitude p prevails inside the core. The stresses and displacement outside the core are taken to be the same as that in an infinite elastic–plastic body containing a spherical cavity under pressure p . These fields have been presented in [17,28].

The relationship between the core pressure p and the plastic zone radius r_p is given by

$$p = D\sigma_0^c \left(\frac{r_p}{a}\right)^{2q} - \frac{B}{q}\sigma_0^c. \quad (\text{A.1})$$

Here, B , q and D are given by

$$B = \frac{(1 - \tan \alpha/3)}{(1 + 2 \tan \alpha/3)}, \quad (\text{A.2})$$

$$q = \frac{\tan \alpha}{(1 + 2 \tan \alpha/3)}, \quad (\text{A.3})$$

$$D = \frac{B}{q} + \frac{2}{3}(1 - \tan \alpha/3). \quad (\text{A.4})$$

The cavity model of indentation assumes that the radial displacement of particles lying on the core boundary during an increment of penetration accom-

modates the volume of material displaced by the indenter. On applying this condition along with the expression for the radial displacement for an internally pressurised spherical cavity, the evolution equation for the plastic zone size r_p with contact radius a is obtained as (see [17]):

$$\frac{\sigma_0^c}{E} \left[2qM \left(\frac{r_p}{a}\right)^{2q-1} - \frac{3L}{2} \left(\frac{r_p}{a}\right)^{s-1} \right] \frac{dr_p}{da} = \frac{a}{2R}. \quad (\text{A.5})$$

Here, L , s and M are given by:

$$L = \frac{2(2q-3)(1-\nu)}{(3-4q\eta)} Dq, \quad s = \frac{3}{2\eta}, \quad (\text{A.6})$$

$$M = L\eta + (1-\nu)(q-1)D + \nu D, \quad (\text{A.7})$$

where

$$\eta = \frac{1}{2} + \frac{\tan \alpha}{3}. \quad (\text{A.8})$$

It can be shown (see [17]) that in the limit as $\alpha \rightarrow 0$, the evolution equation for the plastic zone size (Eq. (A.5)) reduces to that given by Johnson [25]

$$\frac{\sigma_0^c}{E} \left[3(1-\nu) \left(\frac{r_p}{a}\right)^2 - 2(1-2\nu) \frac{a}{r_p} \right] \frac{dr_p}{da} = \frac{a}{2R}. \quad (\text{A.9})$$

Eq. (A.5) or (A.9) can be integrated numerically from the contact radius corresponding to initial yielding, a_y , which is determined as explained by Narasimhan [17] and

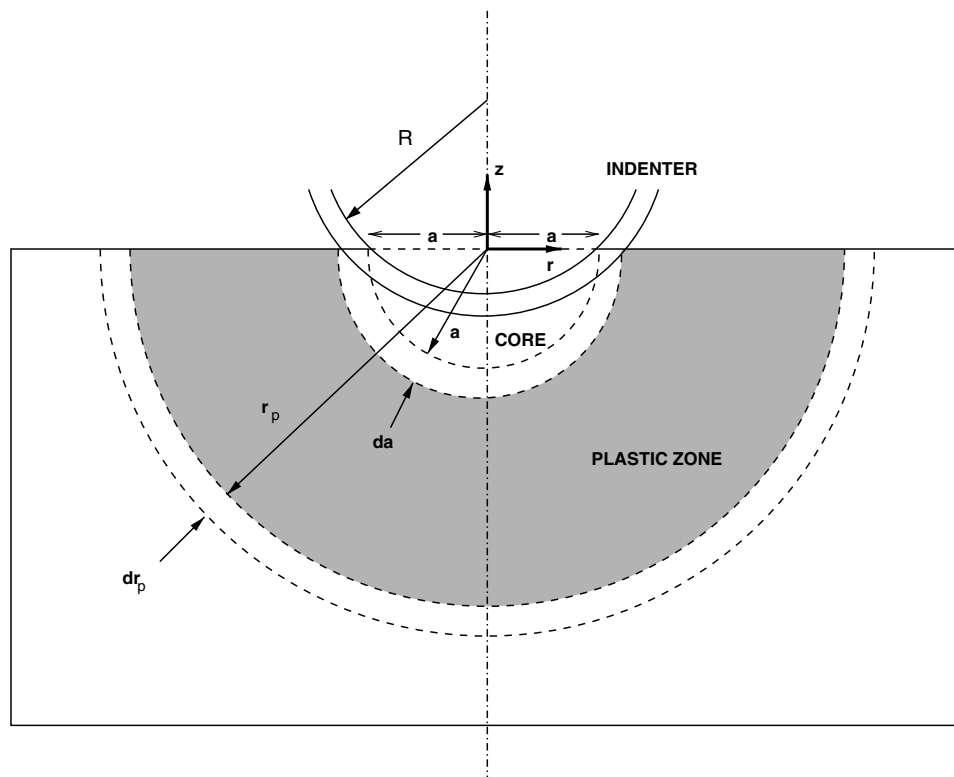


Fig. 10. Schematic illustrating elastic–plastic indentation as idealized by the expanding cavity model. The contact zone is taken to be encased in a hemispherical core of radius a , which in turn is surrounded by a hemispherical plastic zone of radius r_p .

the plastic zone size r_p can be obtained as a function of a . The core pressure p can then be computed from Eq. (A.1).

It must be noted that the stress state immediately beneath the indenter will not be purely hydrostatic. As proposed by Johnson [25], the stresses below the indenter may be approximated with reference to a cylindrical coordinate system (r, θ, z) centered at the point of first contact (see Fig. 10) as follows

$$\sigma_{zz} \simeq -(p + \hat{\sigma}), \quad \sigma_{rr} = \sigma_{\theta\theta} \simeq -(p - \hat{\sigma}/2). \quad (\text{A.10})$$

On substituting this assumed form for the stress components into the yield condition (1), $\hat{\sigma}$ is determined as

$$\hat{\sigma} = \frac{2\sigma_0^c}{3} \left[1 + \tan \alpha \left(\frac{p}{\sigma_0^c} - \frac{1}{3} \right) \right], \quad (\text{A.11})$$

where the core pressure p is obtained as indicated above.

References

- [1] Johnson WL. MRS Bull 1999;24:42.
- [2] Bruck HA, Christman T, Rosakis AJ, Johnson WL. Scripta Metall 1994;30:429.
- [3] Lewandowski JJ, Lowhaphandu P. Philos Mag A 2002;82:3247.
- [4] Spaepen F. Acta Mater 1977;25:407.
- [5] Leamy HJ, Chen HS, Wang TT. Metall Trans 1972;3:699.
- [6] Donovan PE. Acta Metall 1989;37:445.
- [7] Vaidyanathan R, Dao M, Ravichandran G, Suresh S. Acta Mater 2001;49:3781.
- [8] Kimura H, Masumoto T. In: Lubrosky FE, editor. Amorphous Metallic Alloys. London: Butterworth; 1983. p. 187.
- [9] Flores KM, Dauskardt RH. Acta Mater 2001;49:2527.
- [10] Schuh CA, Lund AC. Nat Mater 2003;2:449.
- [11] Lu J, Ravichandran G. J Mater Res 2003;18:2039.
- [12] Sargent PM, Donovan PE. Scripta Mater 1982;16:1207.
- [13] Schuh CA, Nieh TG. J Mater Res 2004;19:46.
- [14] Jana S, Bhowmick R, Kawamura Y, Chattopadhyay K, Ramamurty U, Intermetallics (in press).
- [15] Ramamurty U, Jana S, Kawamura Y, Chattopadhyay K, 2003 (unpublished results).
- [16] Tabor D. Hardness of metals. Oxford: Clarendon press; 1951.
- [17] Narasimhan R. Mech Mater 2004;36:633.
- [18] Johnson KL. J Mech Phys Solids 1970;18:115.
- [19] Giannakopoulos AE, Larsson PL. Mech Mater 1997;25:1.
- [20] ABAQUS/Standard, Theory Manual. Hibbit Karlsson and Sorenson Inc., RI; 1996.
- [21] Oliver WC, Pharr GM. J Mater Res 1992;7:1564.
- [22] Kachanov LM. Fundamentals of the theory of plasticity. Moscow: Mir; 1974.
- [23] Belytshko T, Liu WK, Moran B. Nonlinear finite elements for continua and structures. New York: Wiley; 2000.
- [24] Wriggers P, VuWan T, Stein E. Comput Struct 1990;37:319.
- [25] Johnson KL. Contact mechanics. Cambridge: Cambridge University Press; 1985.
- [26] Fisher-Cripps AC. Introduction to contact mechanics. Berlin: Springer; 2000.
- [27] Sinclair GB, Follansbee PS, Johnson KL. Int J Solids Struct 1985;21:865.
- [28] Chadwick P. Quart J Appl Math 1959;12:52.
- [29] Wright WJ, Saha R, Nix WD. Mater Trans JIM 2001;42:642.
- [30] Bowden PB, Jukes JA. J Mater Sci 1972;7:52.
- [31] Chen WF, Han DJ. Plasticity for structural engineers. Berlin: Springer; 1988.
- [32] Sokolovski VV. Statics of soil media. London: Butterworths Scientific Publications; 1960.
- [33] Kramer D, Huang H, Kriese M, Robach J, Nelson J, Wright A, et al. Acta Mater 1999;47:333.
- [34] Marsh DM. Proc R Soc Lond A 1964;279:420.